

Design Considerations for Plasmonic Photovoltaics

By Vivian E. Ferry, Jeremy N. Munday, and Harry A. Atwater*

This paper reviews the recent research progress in the incorporation of plasmonic nanostructures with photovoltaic devices and the potential for surface plasmon enhanced absorption. We first outline a variety of cell architectures incorporating metal nanostructures. We then review the experimental fabrication methods and measurements to date, as well as systematic theoretical studies of the optimal nanostructure shapes. Finally we discuss photovoltaic absorber materials that could benefit from surface plasmon enhanced absorption.

1. Demand for Inexpensive, Ultrathin Film Photovoltaics

One of the great challenges facing society today is the supply of low-cost, environmentally friendly energy sources that can meet the growing demands of an expanding population. Photovoltaic power has the potential to meet these needs, because the amount of radiation striking the earth's surface is 1.76×10^5 terawatts (TW) and current world usage is estimated at 14 TW.^[1] With respect to other renewable and non-renewable energy resources, however, the cost of photovoltaic modules continues to be high, and cost per Watt remains the driving force behind much of photovoltaics research.

For crystalline Si approximately 50% of this cost is due to the cost of the materials themselves, with the remainder due to cell production and module fabrication.^[2] Si is the dominant commercial solar material to date and is a relatively weak absorber, requiring 200–300 μm of semiconductor material to fully absorb the incident sunlight. This Si must be high quality and defect free so that the generated carriers are not lost before collection. In response, alternative thin-film photovoltaic cells with thicknesses of several micrometers have been developed with potentially lower processing costs.^[3] The most efficient thin films currently employed are cadmium telluride (CdTe), copper indium gallium selenide (CIGS), and amorphous Si (a-Si:H), with the record efficiency of these devices at 19.9% (CIGS).^[4–7] However, the first two of these thin film designs use scarce elements such as Te and In, and at their current efficiency the technology is not scalable to meet world demand.^[8–10] Most photovoltaic materials face a tradeoff between the necessary thickness for

complete optical absorption and the requisite electronic quality for long minority carrier diffusion lengths.

New materials and new cell design concepts that use ultrathin but fully absorbing layers are therefore critical for low-cost, scalable photovoltaics. Besides the benefits of reduced carrier collection lengths, the open circuit voltage (V_{oc}) of a device increases as the layer thickness decreases due to a reduction in bulk recombination.^[11] If all other factors are held constant, including that the active region can be made to absorb all of the incident light, then the overall efficiency of the cell should increase as its thickness decreases. The standard method for enhancing absorption in a solar cell is to employ front or back surface texturing that scatters light in the layer at multiple angles, thereby increasing its path length.^[12–15] Random surface texturing can lead to a maximum enhancement of $4n^2$ at long wavelengths,^[15] where n is the refractive index of the absorber, but the micrometer-sized features are not appropriate for thin film cells where the total film thickness may be only a fraction of a wavelength.

The incorporation of plasmonic nanostructures in photovoltaic devices has the potential to overcome the problem of light trapping for thin films.^[16] Surface plasmons are bound electromagnetic oscillations of electrons at the interface between a metal and a dielectric material, and have attracted attention due to their ability to guide and confine light in small volumes.^[17–19] Recent experimental realizations of plasmon-enhanced Si photovoltaics have found photocurrent enhancements of a factor of 18 at 800 nm, and reports in the literature can be found for other inorganic semiconductors such as GaAs, a-Si:H, CdSe/Si, InGaN/GaN, and InP/InGaAsP, for organic semiconductors such as polythiophene (P3HT) and copper phthalocyanine (CuPC), and for hybrid inorganic-organic devices such as dye sensitized solar cells (DSSC).^[20–32] In parallel, several recent theoretical and simulation publications have focused on systematic exploration of the optimal scattering arrangements.^[33–36]

This paper explores different device architectures for surface plasmon enhanced absorption, current collection, and efficiency in photovoltaics. We begin by discussing the theoretical background of surface plasmons and waveguide-based solar cells, and outline potential device structures. We then review the experimentally realized devices to date and the systematic studies of device design, and examine some of the challenges to designing efficient nanostructures. In the third section we develop one example structure as a case study for design considerations. Finally we discuss unusual absorbers as candidate systems for plasmon enhanced photovoltaics.

* V. E. Ferry, Dr. J. N. Munday, Prof. H. A. Atwater
Thomas J. Watson Laboratories of Applied Physics
California Institute of Technology
Pasadena, California 91125 (USA)
E-mail: haa@caltech.edu

DOI: 10.1002/adma.201000488

2. Design Components for Plasmonic Photovoltaics

2.1. Absorption Enhancements Due to Plasmonic Nanostructures

We discuss a few distinct plasmonic mechanisms for enhancing absorption in solar cells, which together encompass most of the explored devices to date. First, subwavelength metal nanostructures can be used to scatter incident light into a distribution of angles, increasing the path length of the light within the absorbing layer.^[37] This can lead to higher short circuit current densities (J_{sc}), in both relatively thick cells and thin cells on index-matched substrates.^[21,22] The second mechanism uses the scattering center as a means to excite propagating waveguide modes within the thin absorbing layer. The propagating waveguide modes may be either photonic waveguide modes or surface plasmon polariton (SPP) modes, and the scattering center is used to overcome the momentum mismatch between the incident wavevector and that of the waveguide mode.^[20,33–35] As the mode propagates, the power in the waveguide mode will be absorbed partially in the semiconductor layer, thereby exciting electron-hole pairs and enhancing absorption by redirecting the light horizontally. Carrier collection usually occurs in the vertical direction, orthogonal to the absorption path. A third plasmonic mechanism for enhanced absorption results from high near-field intensities associated with the localized surface plasmonic resonance of the particle. Depending on the shape and size of a metallic particle, particular frequencies of optical excitation will result in strongly enhanced fields near the particle. Since the optical absorption is proportional to the field intensities, high local fields lead to increased absorption. The challenge for photovoltaic applications is to design scattering objects with high effective cross sections that are both broadband across the solar spectrum and insensitive to angle of incidence.

The introduction of scattering objects into a solar cell modifies the standard exponential absorption profile. The intensity at a given depth in a cell with a planar surface is related to the incident intensity I_{in} by $I = I_{in}e^{-aL}$; L is the path length of the light in the medium, and a is the absorption coefficient of the material. The simplest architecture for a solar cell employing scattering objects is a conventional, thick device with a sparse array of sub-wavelength metal scatterers deposited on the top, where incident light scatters independently at each scatterer and collective scattering modes are neglected.^[38] We assume minimal transmission $T(\lambda)$, so that the power is either absorbed (in the semiconductor, metal, or supporting layers) or reflected (including back scattering). In the absence of interference between the scattering objects, the fraction of total power absorbed in the semiconductor $A(\lambda)$ is

$$A(\lambda) = \xi Q_{\text{scat}}(\lambda) f_{\text{substrate}}(\lambda) + (1 - \xi Q_{\text{scat}}(\lambda))(1 - R_s(\lambda)), \quad (1)$$

where ξ is the fraction of the surface covered by scatterers, Q_{scat} is the normalized scattering cross section of the nanoparticle relative to its physical size, $f_{\text{substrate}}$ is the fraction of the total scattered light that is forward scattered into the substrate, and $R_s(\lambda)$ is reflection from the semiconductor interface only, in



Vivian E. Ferry is currently a fourth year PhD student at the California Institute of Technology. She earned her BS in chemistry from the University of Chicago in 2006. Her research focuses on the design of plasmonic nanostructures for enhanced absorption in photovoltaics.



Jeremy N. Munday is currently a Postdoctoral Scholar in the Department of Applied Physics at the California Institute of Technology. He earned his PhD and MA in Physics from Harvard University in 2008 and 2005, respectively, and his BS in Physics and Astronomy from Middle Tennessee State University in 2003.

His research interests primarily focus on photovoltaics, plasmonics, and quantum electrodynamic phenomena such as the Casimir effect.



Harry Atwater is currently Howard Hughes Professor and Professor of Applied Physics and Materials Science at the California Institute of Technology. His research interests center around two interwoven research themes: photovoltaics and solar energy; and plasmonics and optical metamaterials. Atwater and his group have been active in photovoltaics research for more than 20 years. Recently they have pioneered a new photovoltaic device, the silicon wire array solar cell, and have developed new fabrication approaches to III-V semiconductor multijunction cells, as well as making advances in plasmonic light absorber structures for III-V compounds and silicon thin films.

the absence of a nanoparticle. For normally incident light the path length of the scattered light is increased to $\frac{L}{\cos(\theta)}$, where θ is the angle between the scattered light and the surface normal. The reflection term $R_s(\lambda)$ is reflection from the semiconductor interface only, in the absence of a nanoparticle.

The normalized quantity Q_{scat} can be calculated from the scattering cross section σ_{scat} using $Q_{\text{scat}} = \frac{\sigma_{\text{scat}}}{\sigma_{\text{geom}}}$, where σ_{geom}

is the geometrical cross section of the object. In the quasistatic limit where the nanoparticles are much smaller than the wavelength of incident light and the field on the particle is uniform, the scattering cross section is given by

$$\sigma_{\text{scat}} = \frac{1}{6\pi} \left(\frac{2\pi}{\lambda} \right)^4 |\alpha|^2, \quad (2)$$

where α is the polarizability of the particle.^[37] For spherical nanoparticles embedded in a semiconductor with permittivity ϵ_s , the polarizability is calculated from

$$\alpha = 4\pi r^3 \frac{\epsilon_m - \epsilon_s}{\epsilon_m + 2\epsilon_s}, \quad (3)$$

where r is the radius of the nanoparticle and ϵ_m is the permittivity of the metal. When $\epsilon_m \approx 2\epsilon_s$ the polarizability is at a maximum and the particle exhibits a dipolar surface plasmon resonance. The quantity Q_{scat} thus depends on both the size of the particle and the local environment, both of which can be used to tune the scattering properties.

The absorption cross section σ_{abs} in the metal scales with the polarizability, as well:

$$\sigma_{\text{abs}} = \frac{2\pi}{\lambda} \text{Im}[\alpha]. \quad (4)$$

For solar cell applications an important design criterion is that $\sigma_{\text{scat}} \gg \sigma_{\text{abs}}$ to keep metallic losses low, because sunlight absorbed in the metal will not contribute to useful carrier generation. In the case of the smallest nanoparticles, $\sigma_{\text{scat}} + \sigma_{\text{abs}} \approx \sigma_{\text{abs}}$ but as the particle size increases σ_{scat} grows and the dipolar plasmon resonance red shifts and broadens. As the size of the nanoparticle approaches λ , both the quasistatic approximation breaks down and multipolar modes contribute to the particle's scattering cross section. All of the equations given above are valid for dielectric particles as well as metallic ones and the difference lies in ϵ_m : dielectric particles have both more modest permittivities than metals and $\text{Re}[\epsilon_s] > 0$, and thus do not exhibit resonant behavior.

This resonant dipolar scattering behavior is not limited to spherical metal nanoparticles; metallic voids exhibit similar behavior, and a wide variety of other nanoshapes can be made including cylinders, hemispheres, core-shell particles, and anisotropic particles. Each different shape of particle will have a different $f_{\text{substrate}}$, so particle shape must be chosen to couple preferentially into the substrate rather than backscatter into free space.^[30]

We now consider the case of an isolated nanoparticle on top of a thin film of absorbing material, as illustrated in **Figure 1** (adapted from^[35]). Incident light is scattered off the object into a distribution of optical modes within the semiconductor. When the semiconductor is surrounded by index contrasting layers this structure can act as a waveguide. A fraction ρ of the power scattered off the nanoparticle will couple to the escape cone (ρ_0) and a fraction ρ_j to each guided mode, so that $\rho_0 + \sum_{j=1}^N \rho_j = 1$, where N is the number of modes in the semiconductor. We call the effective size of the scatterer that couples to each mode the incoupling cross section $\sigma_{\text{inc},j}$, where

$$\sigma_{\text{inc},j} = \sigma_{\text{scat}} f_{\text{substrate}} \rho_j. \quad (5)$$

When normalized by the geometrical size of the object, this gives the normalized incoupling cross section $Q_{\text{inc},j} = \frac{\sigma_{\text{inc},j}}{\sigma_{\text{geom}}}.$ ^[33]

Each of these modes will have a characteristic overlap with the semiconductor that describes the fraction of energy absorbed in the semiconductor, $\Gamma_{s,j}$. For a given mode at one wavelength, the fraction of power absorbed in the semiconductor layer of the cell is given by

$$A_j(\lambda) = \xi Q_{\text{inc},j} \Gamma_{s,j}. \quad (6)$$

The fraction of total power absorbed in the semiconductor as a function of wavelength is then

$$A(\lambda) = \sum_{j=0}^N A_j(\lambda) + (1 - \xi Q_{\text{scat}}(\lambda))(1 - R(\lambda) - T(\lambda)). \quad (7)$$

Until now we have described only the effects of isolated scattering objects. In the limit where the scatterers act completely independently (and there is no effect from collective modes of the scatterers), the scattering objects should be placed ξQ_{scat} apart, effectively covering the entire surface. This case is similar to the first case of particles on a thick cell. The second case, where the absorbing layer is a thin waveguide, is illustrated in **Figure 1**.^[35] After the initial scattering event the propagating modes can re-scatter from the object. A particular mode may continue to propagate past a neighboring scattering object, or it may be rescattered into either the escape cone or the other allowed modes of the structure. The design challenge lies in finding arrays of scatterers that efficiently incouple sunlight to the modes of the cell without increasing the outcoupling of the propagating modes. The opposite limit, where the scatterers are close together and exhibit near field coupling, is outside the scope considered here.

Figure 2 illustrates several possible architectures for integrating scattering objects into photovoltaic devices. Variables include the shape of the scattering center, its relative height in the waveguide, arrangement with respect to other scattering objects, and the use of either dielectric or metallic surrounding layers. For example, the scattering objects may be nanoparticles, gratings, or holes in an otherwise continuous metal film. The shape of the nanostructure is another variable: hemispheres, cylinders, cones, or anisotropic shapes are all possibilities, each with their own Q_{scat} and angular scattering distribution.^[30]

As depicted in **Figure 2a–c** the relative position of these scattering objects within the semiconductor layer may be varied, with scatterers located on top, embedded within, or positioned on the back of the absorber layer. The location of the scattering center can strongly change the coupling fractions ρ_j for each mode. **Figure 2d** illustrates another variable: the arrangement of the scattering objects relative to one another. We show one potential tiling of grooves or ridges, a hexagonal arrangement for efficient and polarization-independent surface coverage. Of course the scattering objects could be tiled in square lattices or more complicated patterns, or arranged in a quasi-random geometry.

The exact structure of the scattering and absorbing layers can also modify both the types of modes excited and their

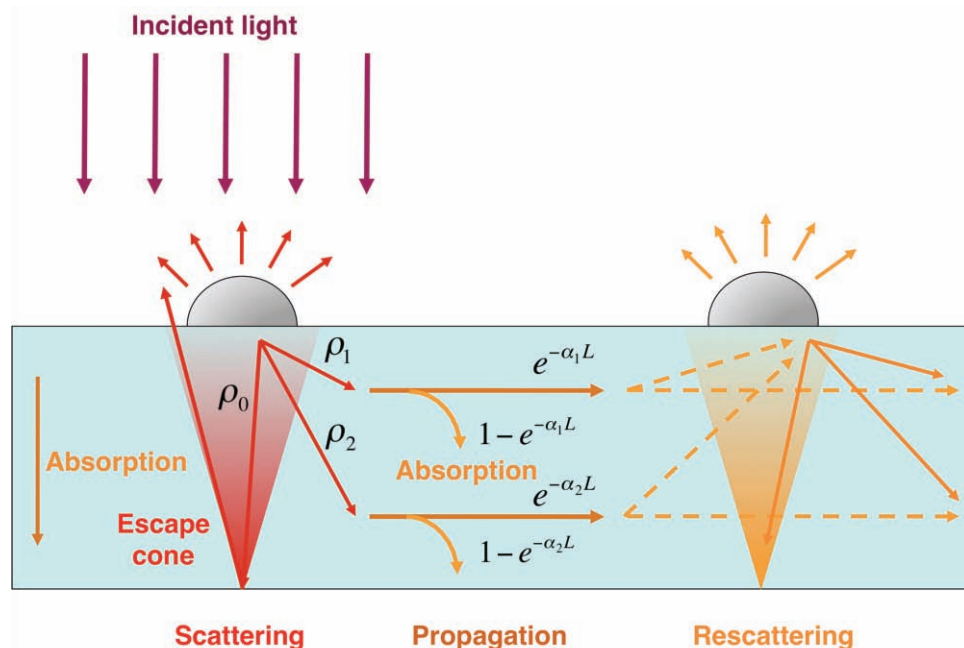


Figure 1. Diffusion model for light propagation inside the solar cell. Incident light is scattered off a scattering object, with a fraction ρ_0 coupling to the escape cone and ρ_1 to each guided mode. The modes propagate a distance L , with appropriate losses in the absorbing layer and cladding materials, until the next scattering object. At the next scattering object the mode is rescattered. Adapted from [35] with permission from the Optical Society of America.

semiconductor overlap Γ_s . The back cladding of the cell could be a metal or a transparent conductor (TC), for example, or a combination of both where the TC acts as a spacer between the semiconductor and the metal, similar to the back contacts of

many thin film Si cells. Ideally this back contact has low optical loss, allowing for waveguiding of modes rather than parasitic absorption. These spacer layers can also be used to tune the spectral scattering of the nanostructure: changing the refractive

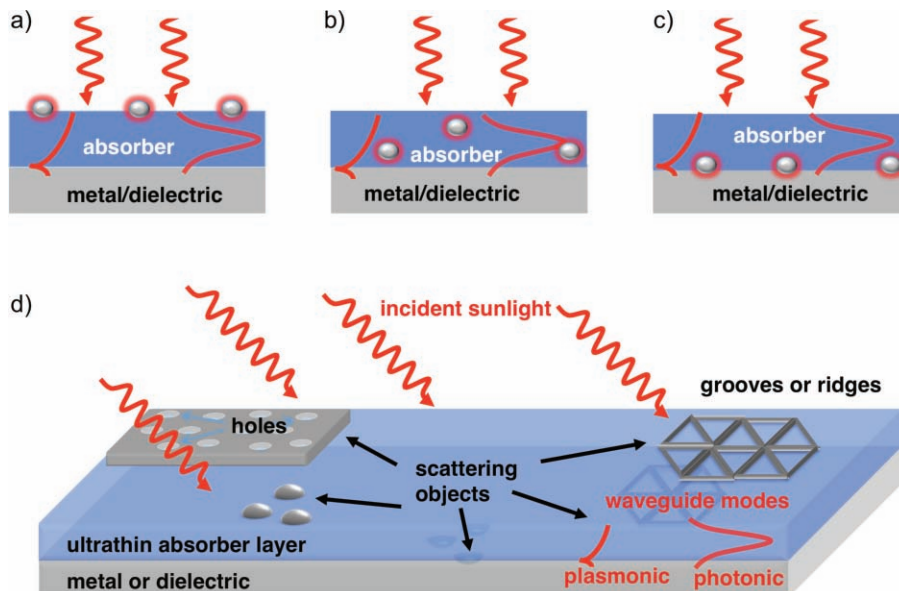


Figure 2. Generalized scatterers for coupling into waveguide modes in a solar cell. Scatterers can consist of particles on top (a), middle (b), or back (c) of the solar cell and could contain layers of metal, dielectrics, transparent conducting oxides, or air on the back surface. Incident sunlight is then scattered into photonic or SPP modes depending on the scattering object and incident wavelength of light. (d) Schematic of a solar cell with various scattering object tilings.

index of the surrounding material will shift the resonant frequencies and change the modal shape.

2.2. Waveguide Modes

The modes excited by the scattering object may be of two general types: waveguide modes that we call “photonic” due to their resemblance to the slab modes of planar dielectric waveguides, or SPP modes supported on the interface of the planar metal film and the second material.^[17,39] When that second material is lossless, the SPP modes can propagate over distances of 10–100 μm before the Ohmic losses in the metal dominate. The SPP modes are tightly confined to the interface, with skin depths in the tens of nanometers. Naturally when the second material is a semiconductor, the power in the mode can be absorbed partially in the semiconductor. Enhanced absorption in the semiconductor may be due to either the photonic or the SPP modes.

By solving Maxwell's equations subject to the appropriate boundary conditions, we obtain the field intensity profiles for the various waveguide modes of a planar multilayer structure. Two independent sets of solutions exist, transverse magnetic (TM) and transverse electric (TE) with their magnetic field and electric field completely in the plane, respectively. Figure 3 shows the modal profiles (calculated from simulation) at 920 nm with both TE and TM polarizations for a 200 nm thick layer of Si with a 60 nm anti-reflective (AR) coating on the top and either air (Figure 3a,b) or 300 nm of Ag (Figure 3c,d) on the back side. These modal profiles represent the power in the mode as a function of position in the waveguide and are normalized to the same integrated power to compare their shapes. In all cases we see that the modes are largely within the Si-AR core and decay more sharply into the surrounding air or Ag. The number of modes present in the waveguide depends

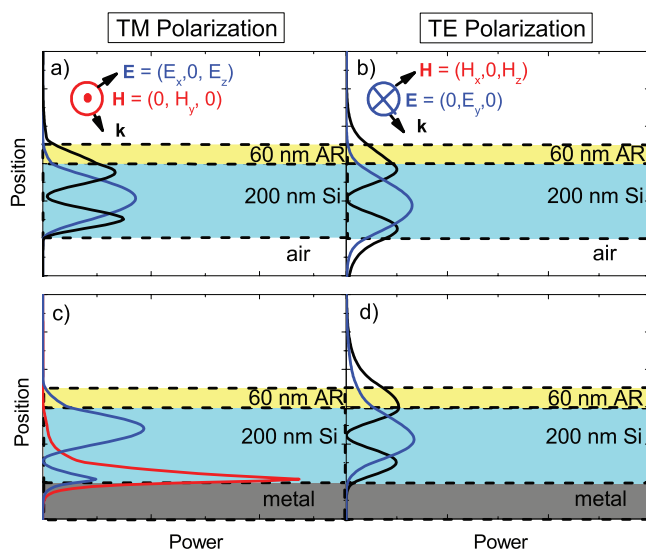


Figure 3. Modal profiles at $\lambda = 920$ nm for TM and TE polarizations, with and without metal back contacts. Profiles are normalized to equivalent power under the curve and are calculated from post-processed finite difference time domain simulation.

on both the thickness of the slab and on the wavelength of the incident light.

By comparing the shapes of the modes we can predict which modes will be most advantageous for optical absorption enhancement in the semiconductor, as discussed in more detail by Saeta et al.^[35] The photonic modes in Figure 3a,b,d have similar shapes to each other, with varying decay outside the semiconductor. From the modal profiles, we expect that the fundamental mode in each case (shown in blue) will lead to the most enhancement due to the absence of nodes within the semiconductor. The higher order mode (in black) suffers from a node nearly in the center of the structure. At shorter wavelengths additional higher order modes are present but these will have diminishing effect on the absorption due to the presence of nodes. We also intuitively expect the TE modes to have higher absorption due to the minimized absorption in the metal. Of course thicker layers will support an increasing number of photonic modes.

With the addition of a metal interface the TE mode changes its shape slightly (Figure 3d), but there is no substantial change in the location of power or in the number of accessible modes. In the TM case (Figure 3c), a fundamentally different type of mode is visible when one of the interfaces is metal: the surface plasmon polariton mode which is tightly confined to the semiconductor-metal interface and decays exponentially from each side of the boundary. The lowest order photonic mode under TM polarization changes shape as well, introducing a node within the Si just above the interface.

To further understand the SPP mode, we consider the field components in a simple two material structure with semi-infinite metal and semiconductor layers. In homogeneous media the solution to Maxwell's equations are plane waves of the form:

$$E(x, z, t) = E_0 e^{i(k_x x - k_z z - \omega t)} \quad (8)$$

$$H(x, z, t) = H_0 e^{i(k_x x - k_z z - \omega t)} \quad (9)$$

where x is the direction of propagation and k_x and k_z are the wave vector components in the x - and z -directions for angular frequency ω . For TM modes, only E_x , E_z , and H_y are non-zero. Enforcing continuity of the tangential component of E (i.e. $E_{x,m} = E_{x,s}$) and the normal component of D (i.e. $\epsilon_m E_{z,m} = \epsilon_s E_{z,s}$) at the interface yields

$$-\frac{k_{z,m}}{k_{z,s}} = \frac{\epsilon_m}{\epsilon_s}, \quad (10)$$

which can be satisfied for a metal interface because $\text{Re}[\epsilon_m] < 0$ and both $\text{Re}[k_{z,m}] > 0$ and $\text{Re}[k_{z,s}] > 0$. Because the H_y component in both materials must satisfy the wave equation, we also have:

$$k_{z,i}^2 = \epsilon_i \left(\frac{\omega}{c} \right)^2 - k_x^2. \quad (11)$$

Combining these relations yields the surface plasmon dispersion relation

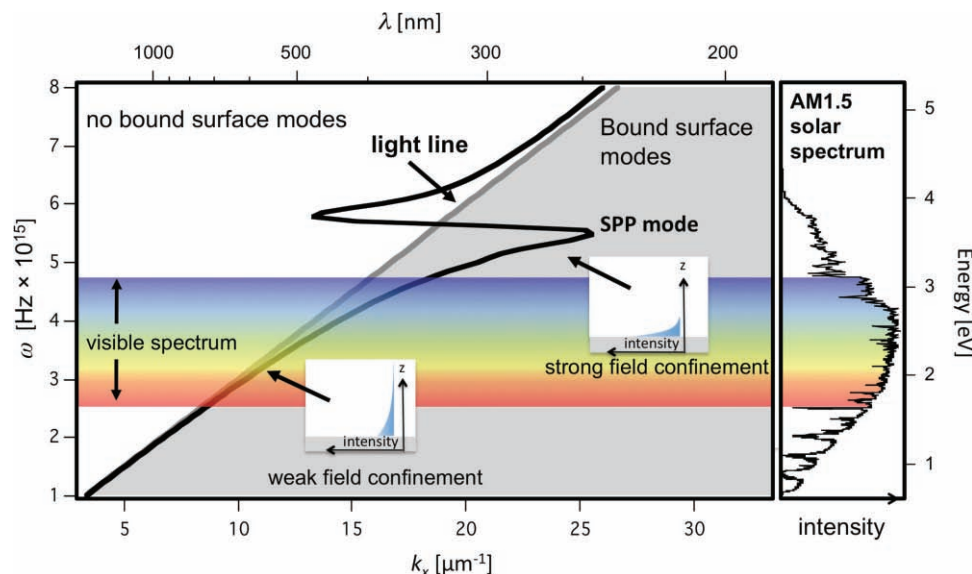


Figure 4. Surface plasmon polariton dispersion relation for an Ag/Air interface. Black (grey) line corresponds to the dispersion relation for the SPP mode (light line). A significant fraction of the solar spectrum (right part of figure) has access to the bound SPP mode.

$$k_x = \frac{\omega}{c} \sqrt{\frac{\epsilon_m \epsilon_s}{\epsilon_m + \epsilon_s}}. \quad (12)$$

Figure 4 shows the dispersion relation for an SPP mode at the Ag/Air interface, with the solar spectrum and visible spectrum highlighted. Modes to the right of the light line, the line describing light propagation in air, are bound to the interface. At low frequency, the SPP modes are close to, but to the right of, the light line. At resonance, where $\epsilon_m \approx -\epsilon_s$, the modes are highly confined with large wave vectors, and their propagation lengths are very short. The position of resonance depends on the optical properties of the metal and the semiconductor, so appropriate material and thickness choices will allow the amount of light confinement to be tailored for the most efficient use.

For the TE case, no bound surface modes exist. Recall that only H_x , H_z , and E_y components are present, and that $E_x = E_z = H_y = 0$ for this case. Enforcing continuity at the interface $z = 0$ for the E_y and H_x terms yields

$$E(z=0) = k_{z,m} + k_{z,s} = 0. \quad (13)$$

Because both $\text{Re}[k_{z,m}] > 0$ and $\text{Re}[k_{z,s}] > 0$, we must have $E_{z=0} = 0$, and thus no surface mode exists under TE polarization.

2.3. Device Performance Benefits for Thin Absorbing Layers

While thin film absorbing layers may suffer from reduced J_{sc} due to a reduction in the number of photons absorbed within the layer, device performance may actually improve due to increased V_{oc} .^[40] In the short diode limit we have

$$V_{oc} = \frac{kT}{q} \ln \left[\frac{J_{sc}}{J_0} + 1 \right], \quad (14)$$

where J_{sc} is the short circuit photocurrent per area and J_0 is the saturation current per area for the cell. The saturation current depends proportionally on the volume of the material, and so decreasing the thickness of material leads to a lower recombination current. If J_{sc} decreases less quickly with thickness than J_0 , then V_{oc} can increase for thinner cells. However, one must also consider the reduced shunt resistance and surface recombination effects in ultra-thin layers.

3. State of the Art: Experimental Results

The most common plasmon enhanced solar cell structure to date consists of metallic nanoparticle scatterers (of various shapes) deposited on top of an already fabricated solar cell. These cells have the advantage that the fabrication process does not have to be substantially modified to incorporate plasmonic scatterers. The disadvantage is that, since the particles are on top, attention must be paid to the density of objects to avoid shadowing. The presence of particles on top also modifies the use of AR coatings, and so any added benefits from nanoparticles must be weighed against the benefits due to conventional antireflection methods.

The first papers to explore the potential of surface plasmons in photovoltaics were published in the late 1990s by Stuart and Hall.^[20,40,41] Their device consisted of a thin silicon-on-insulator (SOI) wafer, where the Si was 165 nm thick, and since the absorbing Si layer was separated from the Si substrate by a layer of SiO_2 , it acts as a thin waveguide. Metal island formation was achieved by depositing a thin metallic film and annealing under N_2 so that the film coalesced into discrete islands. The size and shape of the particles can be tuned to some extent by varying the thickness of the metal layer and the annealing time and temperature, although the patterns

and spacings were irregular. The authors report a photocurrent enhancement as high as 18 at 800 nm with the addition of Ag islands. Since then other groups have extended the island annealing technique on Si and other absorbers. Similar results were noted in 2007, where a photocurrent enhancement of 16 for a 1.25 μm SOI cell due to Ag nanoparticles was reported, with a solar spectrum integrated enhancement of 30%.^[21]

A second fabrication approach uses colloidal Ag and Au nanoparticles as the source of scattering objects. This allows for uniformity of the size and control of the density of particles, although it is difficult to pattern the particles precisely and prevent aggregation. This type of deposition has been used on crystalline Si (c-Si), a-Si, and an InP/InGaAsP quantum well p-i-n structure.^[25,42,43] Other deposition techniques include island formation on transparent conductive oxides for organic photovoltaics, incorporation of metal nanoparticles inside the active layer, electron beam lithography, and electrodeposition.^[44–48]

We have recently utilized a fabrication technique using anodic aluminum oxide (AAO) templates as evaporation masks for the deposition of metallic nanoparticles.^[22,32] For optically thin p-n photovoltaic layers of GaAs (200 nm), that do not support waveguide modes due to an index-matched absorbing substrate, an 8% increase in J_{sc} was observed for Ag nanoparticles.

The AAO templates can be used to controllably and reproducibly deposit metallic particles onto a cell via evaporation through the template (**Figure 5**). The hole density of the template is controlled by the applied voltage during anodization, the hole diameter is controlled by the etch time, and the particle height is controlled by the metal deposition thickness during evaporation.^[48] Upon annealing, hemispherical and conical particles can be formed (**Figure 5d,e**). This procedure allows the particle spacing, shape, and size to be tuned and optimized for a given cell.

Figure 5f shows the experimentally determined external quantum efficiency (EQE) of two thin film GaAs solar cells with either dense or sparse particle arrays normalized to a cell that had not been decorated with particles. For these devices, the EQE for long wavelengths is enhanced while the EQE for short wavelengths is reduced. The addition of Ag nanoparticles to the surface of the cell had two benefits. First, the strong scattering from the plasmonic structures increased the effective optical path of the incident light in the absorber. This increased path length leads to an increase in J_{sc} , as seen in other studies. Second, an increase in the fill factor was found, which is believed to be due to a decrease of the cell's surface sheet resistance arising from the conductivity of the particles. While the nanoparticles yielded improvements for this cell, using a cell design that incorporates a greater refractive index contrast between photovoltaic layers and the substrate layer promises further absorption enhancements due to waveguiding.

We recently reported photocurrent enhancements due to nanostructured metallic back contacts in n-i-p a-Si:H solar cells.^[31] In this case the nanopatterns were fabricated using nanoimprint lithography, a technique that allows for large-area, precisely controlled nanostructures and may be incorporated into roll-to-roll processing methods.^[49] The nanofeatures

are imprinted into sol-gel using substrate conformal imprint lithography, then overcoated with Ag to form the back contact and substrate for growth. The nanopatterned cells had 26% higher J_{sc} than reference cells with a flat back interface, with the main photocurrent enhancement in the red portion of the spectrum. Notably, these nanostructured devices do not suffer from losses on the blue side of the spectrum because the incident sunlight is absorbed in the semiconductor before reaching the back contact scatterers.

In addition to those highlighted here, a number of other devices have been fabricated incorporating gratings, nanocavities, and embedded antennas for near field absorption enhancements.^[26,27,47,50–52]

4. Excitation and Incoupling

The challenge in integrating plasmonics with photovoltaics is in achieving truly broadband scattering and modal excitation. The optimization of nanostructures for plasmon enhanced photovoltaics thus requires systematic study of nanostructure shapes and modal coupling. As outlined earlier, we look at the process of enhancing absorption through coupling to guided modes as an iterative process. First we need the modes of the device with the highest semiconductor overlap Γ_s . Second we need scattering objects with the highest σ_{inc} to efficiently couple incident light to the most advantageous modes. Because both σ_{inc} and Γ_s have spectral dependence, the designs must be optimized to the optical properties of the semiconductor and the power in the solar spectrum. This approach focuses on increasing absorption in the cell (most directly related to J_{sc}), and does not consider additional effects such as the modified spatial distribution of carrier generation and the carrier collection efficiencies. Nevertheless, understanding the achievable levels of absorption is a crucial first step toward designing efficient cells.

4.1. Systematic Studies of Scattering Objects

Much of this work utilizes electromagnetic simulation techniques, which are now comparable in speed and computational resources to many of the conventional photovoltaic modeling tools.^[53,54] We recently compared the predicted semiconductor absorption from simulation to the measured external quantum efficiency of a nanostructured n-i-p a-Si:H cell and found good agreement between simulation and experiment, particularly given the approximation to the real cell geometry used for simulation.^[31] Catchpole et al. have recently calculated the fraction of light scattered into the substrate by a number of metallic shapes, including cylinders, hemispheres, spheres, and an ideal point dipole.^[30] The authors calculate $f_{substrate}$ as described earlier, and find that objects such as cylinders and hemispheres are more efficient scatterers than spheres. The effect is attributed to the shorter average distance between the surface and the dipole moment of the scattering object. Under this model, we might expect the highest enhancements for scattering objects embedded inside the absorbing layer, although these would need to be well-passivated to avoid acting as recombination centers within the cell. Hagglund et al. showed that the strength of the

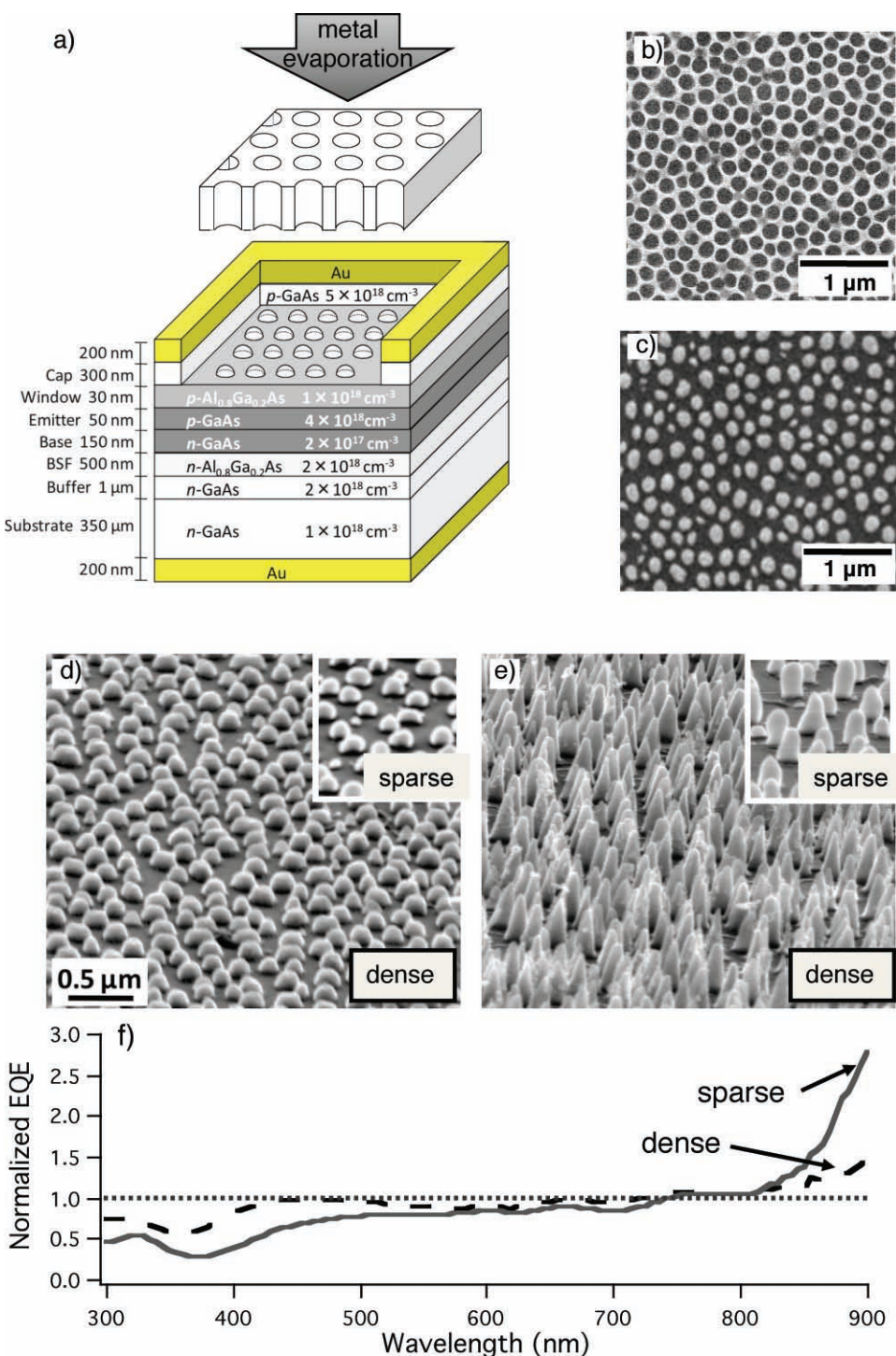


Figure 5. Optically thin GaAs solar cell decorated with Ag nanoparticles deposited by evaporation through an AAO template. (a) Evaporation through the template. (b) SEM image of the AAO template with a hole density of $3.3 \times 10^9 \text{ cm}^{-2}$. (c) SEM image of the deposited nanoparticles using the template of (b). Average particle heights of 55 nm (d) and 220 nm (e) as imaged at 75° from the normal. (f) Normalized external quantum efficiency for two cells with different particle densities. Adapted from reference [22] with permission from the American Institute of Physics.

interaction between cylinders and the underlying substrate can lead to either suppression or enhancement of photocurrent.^[46] Recent modeling work by Beck et al. shows that particles placed on the back of the device have comparable scattering efficiencies

to those on the front.^[55] Placing the particles on the back also avoids the losses in the blue part of the spectrum. Pala et al. analyze the case of a grating on top of a thin film of Si and show that the absorption can be enhanced by 43% in a 50 nm layer.^[34]

Other recent research has looked at the role of particle shape and material experimentally. As described earlier, Nakayama et al. have studied the size and density effects of nanoparticles on GaAs solar cells using AAO templates as evaporation masks and as a means to control the height and density of deposited nanoparticles. The highest efficiency gains were found for dense, high arrays of particles, which are attributed to the interaction of the near-field coupling between particles.^[22] For colloidal spheres, however, it has been shown that aggregation of particles can lead to suppression of photocurrent.^[56] Matheu et al. have compared the scattering responses of metallic nanoparticles and dielectric SiO₂ particles on crystalline silicon substrates, and found that the lower losses in dielectric particles compared to Au particles results in a broader enhancement spectrum.^[42]

4.2. Choice of Metal

Although Ag and Au are the most common plasmonic metals, elements such as Al and Cu have been shown to support surface plasmon resonances in the ultraviolet and visible regions of the spectrum.^[57] Al and Cu are interesting plasmonic materials for photovoltaics because they are less expensive than Ag and Au, but they are also lossier. In general, choice of metal can influence performance by changing the position of resonance, either in nanoparticles or as the back contact in an SPP-based cell. Al and Ag have their resonances in the ultraviolet, while Au and Cu have resonances in the visible portion of the spectrum. For top scatterers made using the AAO templates on GaAs cells, changing from Ag to Al (with roughly constant shape and density of nanoparticles) modifies the photocurrent enhancement across the 400–800 nm range of the visible spectrum significantly, shifting the loss ratios in relation to modified SP resonances.^[38] Calculations on thin GaAs SPP waveguide devices on both Ag and Al showed that Al does shift the SPP resonance to shorter wavelengths but the higher losses in Al decrease the overall absorption enhancements significantly.^[33] The choice of metal may also be influenced by the bandgap of the absorbing layer to provide appropriate overlap between the plasmonic resonance, the absorption spectrum, and the incident solar spectrum (Figure 4). Oxidation of the metal in ambient conditions and the losses due to absorption within the metal should also be considered.^[58]

5. Case Study: Grooves on the Back Contact of an Ultrathin Film Si Cell

5.1. Single Scattering Objects

Besides nanoparticles, strong scattering and incoupling can be observed from metallic strips or gratings. We have recently analyzed the incoupling cross sections for the limiting case of a grating, a single subwavelength groove, structured into the back contact of a Si solar cell.^[33] The spectral dependence of σ_{inc} can be determined by three tunable factors: resonances of the groove, Fabry-Perot resonances within the thickness of

the film, and the planar SPP resonances due to the particular choices of materials. At any of these resonant conditions, the fields in the vicinity of the scattering object are high and there is increased incoupling into propagating modes.

We use finite-difference time domain (FDTD) simulation combined with a post-processing modal filtering technique to separate the $\sigma_{\text{inc},j}$. The resonances mentioned above affect incoupling into the different types of modes in different ways. Near SPP resonance, for example, high local fields in the vicinity of the scattering object lead to increased coupling into the photonic modes, whereas the SPP mode has low group velocity at this frequency and is tightly bound to the vicinity of the scatterer. Near $\lambda = 1100$ nm the metallic grooves exhibit dipole resonances similar to that of nanoparticles, and the strength of this resonance affects coupling to the SPP modes more than the photonic modes.

The placement of the scattering object within the device was also found to affect the relative coupling fractions to the individual modes. The relative coupling to different modes has recently been described for dipoles embedded in a semiconductor layer by Saeta et al. and Hryciw et al.^[35,59] Intuitively, the coupling fractions between the dipole and a given mode scale with the magnitude squared of the field component parallel to the dipole at the same height as the dipole. Furthermore, for high absorption enhancements the dipole coupling to the escape cone must be minimized.

Rather than pure dipoles, our simulation uses more realistic but dipole-like scatterers such as ridges and grooves. There is a substantial difference between metallic ridges on the back contact (sticking up into the absorber) and their inverse, metallic grooves (coming out the back of the absorber). For example, at $\lambda = 1100$ nm, the groove has a total incoupling cross section of 0.35 μm , with 43% of the incoupled power in photonic modes ($\sigma_{\text{inc,phot}} = 0.15 \mu\text{m}$), whereas the ridge has a total incoupling cross section of 0.52 μm with 96% of the incoupled power in photonic modes ($\sigma_{\text{inc,phot}} = 0.5 \mu\text{m}$). We attribute this difference to the relative position of the dipole moment of the scattering object.

For single 100 nm-wide scattering objects in a 10 μm area, we calculated absorption enhancements up to a factor of 2. We calculated absorption enhancements as a function of angle of incidence (0–60°) since a highly performing solar cell will be insensitive to the changing position of the sun. The positions of the Fabry-Perot resonances change as the angle of incidence changes, so absorption enhancement is a more appropriate figure of merit than modal incoupling fractions. At all angles, the enhancements are ≥ 1 . At the four frequencies monitored in the 700–1000 nm wavelength range the enhancements are isotropic, confirming that single objects can act as broad-angle incouplers. Naturally as the number of grooves at close pitch increases the angle selectivity increases as well.

5.2. Arrays of Scattering Objects

The case of multiple scattering objects builds on our previous work,^[33] where we analyzed the incoupling cross sections for each mode and the overall absorption enhancements due to single metallic scattering objects on a metal film back contact.

Here we discuss the opposite limiting case, where the scatterers are close together and there is modal interference. We also expand our model to include antireflective coatings and consider the effects of polarization on the observed enhancements. Although the calculations here are for crystalline Si, the factors affecting incoupling and the method are general to other semiconductors. The example given here is not a fully optimized device design, but is instead intended as an example of our model and the considerations for future extensions.

The simulated device consists of 200 nm of Si on 300 nm of Ag, with a 60 nm AR coating on top of the Si. The AR coating has the refractive index of TiO₂, but is lossless. The basic scattering object considered is a 100 nm wide by 50 nm tall metallic ridge off the back of the cell into the semiconductor, as drawn in the insets of Figure 6. These ridges are spaced either widely enough to act independently (6 μm) or closely together (300 nm). The absorption enhancement is defined relative to a planar slab of 200 nm of Si on Ag. Our source is a normally incident plane wave, and we study the range of incident wavelengths from 400 to 1100 nm where Si is strongly absorbing. As our simulations are 2D, the ridge is assumed to be semi-infinite along the direction of the grating.

The average time-harmonic power absorbed in the semiconductor is given by the divergence of the Poynting vector:^[60]

$$\nabla \cdot S = \frac{1}{2} \int (\omega \epsilon_s'' |E|_s^2 + \omega \mu_s'' |H|_s^2) dx dz. \quad (15)$$

$|E|_s^2$ and $|H|_s^2$ are the magnitudes of the electric and magnetic fields in the semiconductor, respectively, and μ_s'' is the imaginary part of the permeability. In our structure $\mu_n'' = 0$ everywhere, so this term drops out:

$$\nabla \cdot S = \frac{1}{2} \int \omega \epsilon_s'' |E|_s^2 dx dz. \quad (16)$$

The enhancement factor is the ratio of the total absorption in the semiconductor with nanostructures cut into the Si to the total absorption in a planar film. Of course the amount of Si in the nanostructured device is reduced relative to the control device, but we show here that the enhanced absorption benefits

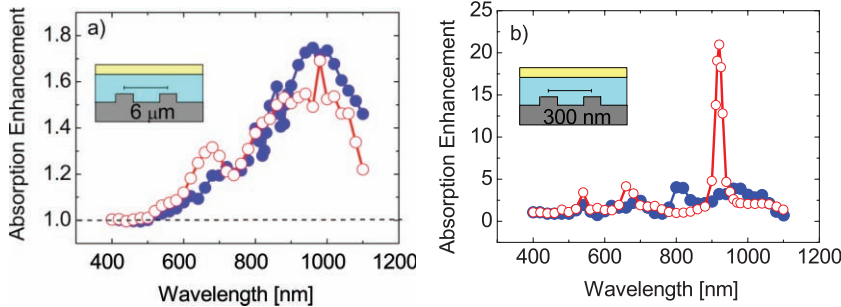


Figure 6. Calculated absorption enhancements for nanostructured c-Si cells with an Ag back contact and an antireflection coating. The Si is 200 nm thick, and the ridges are 100 nm wide and 50 nm tall. Absorption enhancements are relative to an identical structure with a planar Si/Ag interface. In the left panel the scatterers are separated by 6 μm pitch, and in the right by 300 nm. The red (open symbol) curves are for TE polarization, and the blue (closed symbols) are for TM polarization. The dashed lines is at an absorption enhancement = 1, i.e., the case where the absorption is the same as in the planar reference structure.

from nanostructuring outweigh the losses from the slight material reduction.

Figure 6 shows the calculated absorption enhancements for two different spacings of ridges under both polarizations. Figure 6a show the case where the ridges are sparsely spaced, at 6 μm, and Figure 6b shows when they are close together at 300 nm pitch. The dotted line in Figure 6 is at absorption enhancement of 1, which corresponds to the case where the nanostructured device has the same total absorption as the planar reference structure. Note that the y-axes are different in each panel; the sparse pitch axis runs to 2.0 (double the absorption of the planar cell), whereas the grating absorption enhancement runs an order of magnitude higher, to 25.

Comparing the 6 μm spacing to the 300 nm spacing for either polarization shows the trend we expect: gratings with a close pitch are more sensitive to wavelength, with narrower spectral features and wider variation in enhancement across the spectral range. Recall that for TM polarized light incident on our structure, SPPs can be excited, whereas for TE polarized incident light they cannot. In all four cases the enhancements are largest in the weakly absorbing regime of the spectrum, with a broad resonance centered around 1000 nm that we attribute to the magnetic dipole resonance of the ridge. Notably in the sparse cases, although there are regions that show very little enhancement (400–500 nm), the absorption enhancement factors are always above 1. The enhancements reach up to 80% (a factor of 1.8) for the TM case and 70% (1.7) for the TE case.

Many of the features from the 6 μm pitch are exaggerated in the denser system, although new features due to interference are introduced. The magnitude of the variation is clearly larger for gratings, and there are some wavelengths where the enhancements are well below one. However, when the enhancements are averaged over the weighted solar spectrum the gratings on average perform better than the 6 μm pitch structures. In the TM case, the 300 nm pitch grating increases absorption by 22%, whereas the 6 μm pitch structure increases absorption by 6%. In the TE case the 300 nm pitch grating increases absorption by 50%, and the 6 μm pitch structure by 8%. Higher integrated enhancements could be obtained by further optimizing the geometry and pitch of these structures to regions of the solar spectrum with significant power.

Because these devices have unusual absorption profiles, it is not straightforward to determine the optimal location for junctions to collect the generated carriers. Rather than considering only the total power absorbed in the semiconductor, we have extended our calculations to map the electron generation rates throughout the structure. The generation rate is calculated using a spectral weighting term Γ_{solar} and is given by:

$$G_{\text{opt}} = \int \frac{\epsilon_s'' |E|_s^2}{2\hbar} \Gamma_{\text{solar}} dV. \quad (17)$$

These electron generation map profiles are illustrated in Figure 7. Only the generation in the semiconductor is shown, below $x = -1$ is Ag (or air), and above $x = -0.8$ is an AR

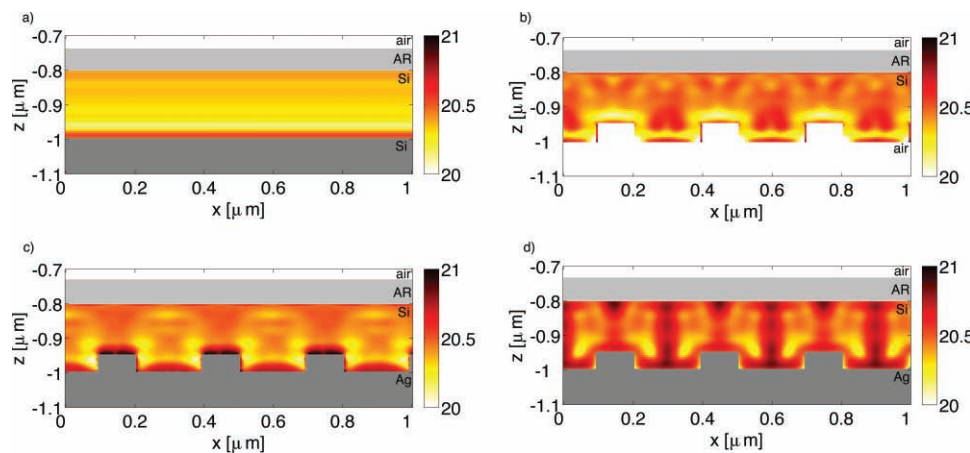


Figure 7. Calculated electron generation rates for nanostructured Si cells. The scale is logarithmic and is given in electrons per cm^3 per second. The arrays are periodic (300 nm) with a sub-section illustrated; each ridge is 100 nm wide (x) and 50 nm tall (z). (a) Flat interface of Si and Ag, TM polarization, (b) grating structure on Si/air interface, TM polarization, (c) grating structure on Si/Ag interface, TM polarization, (d) grating structure on Si/Ag interface, TE polarization.

coating and then air. The color scale is logarithmic, with generation rates mostly in the 10^{20} to 10^{21} electrons per cm^3 per second range. Figure 7a shows the electron distribution for a planar interface. The bands of varying absorption strength are due to the Fabry-Perot resonances within the film, which are strongly present at some wavelengths, but appear reduced in strength when summed over the whole range. Figure 7b shows the TM polarized case with air on the back interface (and hence no SPP excitation), while Figure 7c,d shows the generation rates for the Ag grating case from Figure 6 under TM and TE polarization.

The dense periodic arrays of nanostructures (Figure 7b-d) all show the interference effects between the scattering objects quite strongly; the generation rates are periodic, with regions of high generation concentrated in the “cavity” between the ridges. Figure 7b, in contrast to the others, has lower generation rates around the scattering objects and more concentrated generation in the bulk. Figure 7c, the case with metal under TM polarization, shows very high generation rates near the metallic surface, consistent with SPP excitation and the high fields associated with subwavelength metal nanostructures. The TE case also has high generation in the vicinity of the particle, but its highest bands are in the cavity between centers. This emphasizes the need for contact design near the metallic interfaces to efficiently collect generated carriers.

6. Unconventional Materials for Ultrathin Photovoltaics

The potential to use ultrathin absorber layers in these new architectures opens up a wide range of candidate materials that are unsuitable for bulk devices. Materials such as earth abundant and polycrystalline semiconductors, quantum dots and wells, and molecular absorbers could all stand to benefit from a reduction in thickness. All of the devices illustrated in

Figure 8 are meant as examples of unconventional absorbers in ultrathin configurations rather than strict device architectures. The light trapping designs, as discussed earlier, are amenable to the inclusion of spacer layers, passivation layers, window layers, and other functional materials.

6.1. Earth Abundant and Polycrystalline Semiconductors

Many of the materials used in current thin film photovoltaic technologies, such as CdTe and CIGS, include elements that are among the rarest materials on earth. Tellurium, for example, is one of the nine rarest metals on earth, with concentrations between 1–5 parts per billion in the crust. Because these elements are scarce they are usually isolated as byproducts of mineral purification for other more common elements. For example, Se and Te are produced largely from Cu mining, and In is produced from Zn mining.^[8] As demand increases for these elements in technological applications, such as the use of In for digital displays, the market prices for these rare elements may rise.

The reduction of feedstock materials can help circumvent problems associated with the limited abundance of materials desirable for solar cells. Several studies have examined the material abundance limits for the most common thin film technologies.^[9,10] The estimates discussed here show how improved light trapping (and a concomitant reduction in cell thickness) modifies the material abundance constraints on scalability. We consider single junction cells without additional layers (such as window layers), with all of the material utilized for energy production. Since the costs of extraction can vary due to demand, we consider only the abundance of the material rather than the cost of mining and purification. We also do not consider economic reserves, only annual production.

Currently, PV cells make up a very small fraction of the world's total energy portfolio (<<1%); however, as the demand

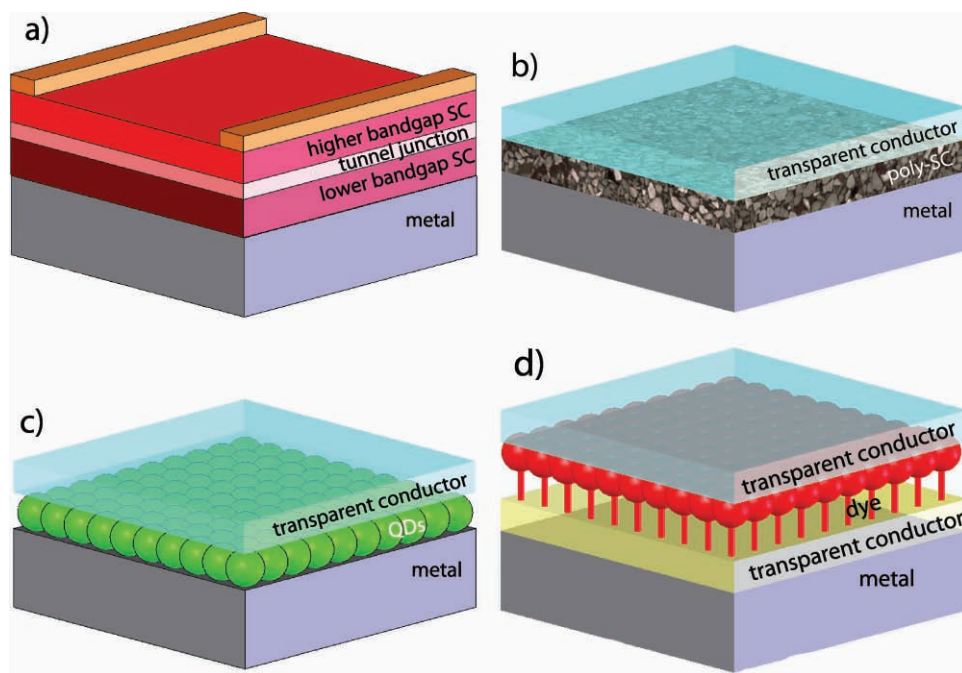


Figure 8. Candidate materials for future photovoltaic devices with ultrathin absorbing layers enhanced via waveguide mode excitation. (a) Multijunction cell consisting of different bandgap semiconductors separated by a tunnel junction, with total thickness < 100 nm. (b) Cell with polycrystalline absorbers, between a metallic back contact and a transparent conducting oxide front contact c) cell with monolayers of quantum dot absorbers, d) cell with monolayers of molecular or organic absorbers.

for renewable energy increases, PV can expect marked growth. We calculate a mass/power for each of the cells listed in Table 1 under different light trapping scenarios, and use this to estimate the amount of material necessary to meet different energy demands. We estimate a thickness under standard light

absorption for each cell by setting the thickness to approximate current production values ($200\ \mu\text{m}$ for c-Si and $3\ \mu\text{m}$ for all other materials). The mass/power (m/P) ratio for each element is given by $\frac{\text{m}}{\text{P}} = \frac{tp}{IA\eta}$ where t is the thickness of the cell, ρ is the density of the element, I is the incident flux ($1000\ \text{W}/\text{m}^2$), A the

Table 1. Current world production of feedstock materials needed for common PV cells. Without increased feedstock production and recycling, many standard PV technologies cannot sustain significant increases in PV demand. Incorporation of ultrathin-film techniques would enable large-scale production of any of the above cells. The bold numbers correspond to consumption of feedstock materials that surpass current production.

Feedstock Material	Current World Production [*] [1000s of tons/yr]	PV Feedstock Consumption for Production of 1.5 Gigawatt/yr (approx. total 2005 PV) [1000s of tons/yr]		PV Feedstock Consumption for Production of 50 Gigawatt/yr [1000s of tons/yr]	
		Standard PV Technology	Ultrathin PV	Standard PV Technology	Ultrathin PV
Si (c-Si)		15		180	18
(a-Si)	1140	0.10		5.4	0.54
Cd (CdTe)	20.8	0.14		7.2	0.72
Te (CdTe)	0.128 ^{**}	0.10		5.2	0.52
Ga (GaAs)	95	0.17		2.2	0.22
(CIGS)		0.016		0.92	0.092
As (GaAs)	53.5	0.17		2.1	0.21
In (CIGS)	0.568	0.019		1.1	0.11
Se (CIGS)	1.59 ^{**}	0.051		3.0	0.30

* World production data taken from US Geological Survey Material Commodity Summaries 2006–2009. ** Excludes US production, which is not reported.

cell area, and η the cell efficiency. For simplicity, we assume that the efficiencies remain near that of current production modules.

As PV power comes into production, the first modules will require materials entirely from feedstock consumption. After year two, however, the lifetime of the cells and recycling of materials becomes important. The scenario outlined here looks only at the initial production. The second column of Table 1 shows current world production of the various PV feedstock materials based mainly on USGS estimates. The third column shows the feedstock consumption to produce 1.5 GW/year, approximately the amount of PV power produced by the US in 2005. In the fourth section of Table 1 we project the amounts of material required to reach 50 GW/year production of new PV. Under the same thickness requirements, there are feedstock limitations to Te, In, and Se. Improved light trapping that reduces the thickness of the cell to one tenth its previous value (with the same efficiency) removes the limitations for In and Se, although Te production is still an issue. Ultrathin film photovoltaic devices are also promising for lower quality materials such as nanocrystalline or amorphous solids because the device performance of these cells are limited by carrier collection.

6.2. Quantum Structures

Quantum confined semiconductor structures, such as quantum dots or quantum wells, are interesting materials for photovoltaics because their bandgaps are tunable across a wide range of the visible spectrum. When the size of the structure is smaller than the bulk exciton Bohr radius, the energy levels of the semiconductor are discrete rather than continuous, and their spacing depends on the size of the structure. In the case of CdSe quantum dots, for example, the bandgap of the dot is tunable across the visible, from 400 to 700 nm. Other II-VI semiconductors such as PbS and PbSe have bandgaps in the near infrared.^[61] Individual quantum well absorbing layers could be stacked on top of each other, similar to a multijunction photovoltaic device. The bandgap of each well is tunable as the width of the well is changed, meaning that the bandgap of each layer can be tuned individually without concern for lattice matching.^[62]

Although the absorption of these quantum confined structures is well matched to the solar spectrum, making efficient photovoltaics has been challenging. CdSe quantum dots blended with conducting polymers have reached efficiencies of 2%, and fully inorganic cells have reached efficiencies of 3%.^[63] One of the limiting factors is the carrier transport through the quantum dot layer, and the highest efficiency cells to date use elongated nanorods to improve transport.^[64]

Devices with thicknesses of a few monolayers thus have the potential for higher efficiencies, because the carriers only need to be extracted from a single layer. It has previously been shown that bulk-like absorption due to SPPs is feasible in ultrathin films of CdSe quantum dots. For a bare Ag film, the launched SPP propagates for 25 μm , but when overcoated with a thin layer of CdSe QDs and illuminated above the bandgap ($\lambda = 514.5 \text{ nm}$) the absorption length is shortened to 1 μm . The

mode overlap of the SPP with the CdSe layer is calculated at $\Gamma = 0.25$. SPPs with energy below the bandgap of CdSe are not absorbed ($\lambda = 1426 \text{ nm}$), and the propagation lengths remain long.^[65]

A solar cell could be imagined to work under a similar mechanism, as illustrated in Figure 8c where a few monolayers of QDs are sandwiched between contacts. Similar sandwich structures using the metal as a Schottky contact have been demonstrated with film thicknesses mainly in the 100–300 nm range.^[66,67] Because the modal overlap fractions are high, this is an example of a device where SPP modes may be more advantageous than photonic mode excitation due to the reduction of thickness afforded by SPP modes.

6.3. Molecular Absorbers

Dye sensitized solar cells and molecular absorbers are another class of attractive materials for plasmonic enhancement. Dye sensitized cells typically use a molecular dye, normally ruthenium-polypyridine derivatives, as sensitizers which inject electrons into a porous TiO₂ layer for electron transport. Efficiencies of about 11% have been reported.^[68] TiO₂ has a high bandgap and absorbs only in the ultraviolet, so the dye layer must be thick enough to absorb a significant fraction of the incident light. The hybrid design thus combines the carrier transport properties of the TiO₂ with the optical absorption properties of the dye.

In addition to dye-based cells, photovoltaic devices based on polymers and small molecules could benefit from increased absorption in small volumes, as depicted in Figure 8d. Nanoantenna based cells, where the absorption is increased due to the high electromagnetic intensity in the near-field of the antenna, have also shown promise. The strong absorption of these materials makes them promising for unconventional device architectures.

7. Conclusions and Outlook

The field of plasmon-enhanced photovoltaics is rapidly expanding, as the light localization properties of metallic nanostructures can be used to reduce layer thicknesses and potentially expand the set of usable absorber materials. Enhanced absorption in semiconductors using plasmonic scatterers offer several advantages relative to standard cell processes. First, most industry AR coatings are optimized for the peak of the solar spectrum, and are often ineffective in long-wavelength regions. The incorporation of plasmonic scatterers on the top surface offers a different type of AR coating, which could be used either in conjunction with or in place of standard coatings. Second, many of the thin film cells fabricated today use roughened back contacts as a means to scatter the long wavelength sunlight and increase absorption. Designed, regular nanopatterning offers an alternative method to precisely couple the incident light into the most beneficial propagating waveguide modes.

The cell architectures illustrated in this paper are meant to show the wide parameter space available to the optimization

of plasmonic scatterers. Several of these architectures involve relatively little perturbation to conventional cell architectures: adding nanoparticle scatterers to the top surface or nanostructures to an existing back contact, for example. Other more unusual designs could be envisioned that account for the changes in the generation rate profiles due to modal propagation, or use unusual absorbing materials in ultrathin film configurations. In either case, the ability of plasmonic nanostructures to enhance absorption in photovoltaic devices warrants exploration of new device architectures and materials systems.

Acknowledgements

We are grateful to Michael Kelzenberg, Domenico Pacifici, Albert Polman, Imogen M. Pryce, Peter N. Saeta, Luke A. Sweatlock, and Marc A. Verschueren for useful discussions. This work was supported by the Office of Energy Efficiency and Renewable Energy, U.S. Department of Energy under Grant No. DE-FG36-08GO18006.

Received: February 8, 2010

Published online: September 2, 2010

- [1] N. S. Lewis, *MRS Bull.* **2007**, *32*, 808.
- [2] W. Koch, A. L. Endros, D. Franke, C. Habler, J. P. Kalejs, H. J. Moller, *Bulk Crystal Growth and Wafering for PV* in *Handbook of Photovoltaic Science and Engineering*, John Wiley & Sons **2003**.
- [3] M. A. Green, *Third Generation Photovoltaics: Advanced Solar Energy Conversion*, Springer **2005**.
- [4] M. J. Keevers, T. L. Young, U. Schubert, M. A. Green, in *22nd European Photovoltaic Solar Energy Conference*, Milan **2007**.
- [5] X. Wu, J. C. Keane, R. G. Dhere, C. DeHart, A. Duda, T. A. Gessert, S. Asher, D. H. Levi, P. Sheldon, in *17th European Photovoltaic Solar Energy Conference*, Munich **2001**, pp. 995–1000.
- [6] A. Romeo, A. Terheggen, D. Abou-Ras, D. L. Batzner, F. J. Haug, M. Kalin, D. Rudmann, A. N. Tiwari, *Prog. Photovoltaics* **2004**, *12*, 93.
- [7] M. A. Contreras, B. Egaas, K. Ramanathan, J. Hiltner, A. Swartzlander, F. Hasoon, R. Nouvi, *Prog. Photovoltaics* **1999**, *7*, 311.
- [8] U. S. Geological Survey: Mineral commodity summaries 2009, U. S. Geological Survey, Washington DC **2009**.
- [9] B. A. Andersson, *Prog. Photovoltaics* **2000**, *8*, 61.
- [10] C. Wadia, A. P. Alivisatos, D. M. Kammen, *Environ. Sci. Technol.* **2009**, *43*, 2072.
- [11] S. M. Sze, K. K. Ng, *Physics of Semiconductor Devices*. John Wiley & Sons, New York **2007**.
- [12] M. A. Green, *IEEE Trans. Electron Devices* **1984**, *31*, 671.
- [13] P. Campbell, M. A. Green, *J. Appl. Phys.* **1987**, *62*, 243.
- [14] H. R. Stuart, D. G. Hall, *J. Opt. Soc. Am. A* **1997**, *14*, 3001.
- [15] E. Yablonovitch, G. D. Cody, *IEEE Trans. Electron Devices* **1982**, *29*, 300.
- [16] H. A. Atwater, A. Polman, *Nat. Mater.* **2010**, *9*, 205.
- [17] H. Raether, *Springer Tracks Mod. Phys.* **1988**, *111*, 1.
- [18] K. R. Catchpole, A. Polman, *Opt. Exp.* **2008**, *16*, 21793.
- [19] S. Maier, *Plasmonics: Fundamentals and Applications*, Springer, New York **2007**.
- [20] H. R. Stuart, D. G. Hall, *Appl. Phys. Lett.* **1998**, *73*, 3815.
- [21] S. Pillai, K. R. Catchpole, T. Trupke, M. A. Green, *J. Appl. Phys.* **2007**, *101*, 093105.
- [22] K. Nakayama, K. Tanabe, H. A. Atwater, *Appl. Phys. Lett.* **2008**, *93*, 121904.
- [23] D. Derkacs, S. H. Lim, P. Matheu, W. Mar, E. T. Yu, *Appl. Phys. Lett.* **2006**, *89*, 093103.
- [24] R. B. Konda, R. Mundle, H. Mustafa, O. Bamiduro, A. K. Pradhan, U. N. Roy, Y. Cui, A. Burger, *Appl. Phys. Lett.* **2007**, *91*, 191111.
- [25] D. Derkacs, W. V. Chen, P. M. Matheu, S. H. Lim, P. K. L. Yu, E. T. Yu, *Appl. Phys. Lett.* **2008**, *93*, 091107.
- [26] A. J. Morfa, K. L. Rowlen, T. H. Reilly III, M. J. Romero, J. van de Lagemaat, *Appl. Phys. Lett.* **2008**, *92*, 013504.
- [27] M. Westphalen, U. Kreibig, J. Rostalski, H. Lüth, D. Meissner, *Sol. Energy Mat. & Sol. Cells* **2000**, *61*, 97.
- [28] C. Hagglund, M. Züch, B. Kasemo, *Appl. Phys. Lett.* **2008**, *92*, 013113.
- [29] C. Wen, K. Ishikawa, M. Kishima, K. Yamada, *Sol. Energy Mat. & Sol. Cells* **2000**, *61*, 339.
- [30] K. R. Catchpole, A. Polman, *Appl. Phys. Lett.* **2008**, *93*, 191113.
- [31] V. E. Ferry, M. A. Verschueren, H. B. T. Li, R. E. I. Schropp, H. A. Atwater, A. Polman, *Appl. Phys. Lett.* **2009**, *95*, 183503.
- [32] I. M. Pryce, D. D. Koleske, A. J. Fischer, H. A. Atwater, *Appl. Phys. Lett.* **2010**, accepted.
- [33] V. E. Ferry, L. A. Sweatlock, D. Pacifici, H. A. Atwater, *Nano Lett.* **2008**, *8*, 4391.
- [34] R. A. Pala, J. White, E. Barnard, J. Liu, M. L. Brongersma, *Adv. Mat.* **2008**, *21*, 3504.
- [35] P. N. Saeta, V. E. Ferry, D. Pacifici, J. N. Munday, H. A. Atwater, *Opt. Exp.* **2009**, *17*, 20975.
- [36] C. Hagglund, B. Kasemo, *Opt. Exp.* **2009**, *17*, 11944.
- [37] C. F. Bohren, D. R. Huffman, *Absorption and Scattering of Light by Small Particles*, John Wiley & Sons, New York **1983**.
- [38] K. Tanabe, K. Nakayama, H. A. Atwater, in *Proceedings of 33rd IEEE Photovoltaic Specialists Conference*, IEEE **2008**.
- [39] J. A. Dionne, L. A. Sweatlock, H. A. Atwater, A. Polman, *Phys. Rev. B* **2005**, *72*, 075405.
- [40] H. R. Stuart, D. G. Hall, *Appl. Phys. Lett.* **1996**, *69*, 2327.
- [41] H. R. Stuart, D. G. Hall, *Phys. Rev. Lett.* **1998**, *80*, 5663.
- [42] P. Matheu, S. H. Lim, D. Derkacs, C. McPheeers, E. T. Yu, *Appl. Phys. Lett.* **2008**, *93*, 13108.
- [43] D. M. Schaadt, B. Feng, E. T. Yu, *Appl. Phys. Lett.* **2005**, *86*, 063106.
- [44] B. P. Rand, P. Peumans, S. R. Forrest, *J. Appl. Phys.* **2004**, *96*, 7519.
- [45] M. Kirkengen, J. Bergli, Y. M. Galperin, *J. Appl. Phys.* **2007**, *102*, 093713.
- [46] C. Hagglund, M. Zach, G. Petersson, B. Kasemo, *App. Phys. Lett.* **2008**, *92*, 053110.
- [47] S.-S. Kim, S.-I. Na, J. Jo, D.-Y. Kim, Y.-C. Nah, *Appl. Phys. Lett.* **2008**, *93*, 073307.
- [48] H. Masuda, M. Satoh, *Jpn. J. Appl. Phys. Phys. 2* **1996**, *35*, L126.
- [49] M. Verschueren, H. van Sprang, in *Mater. Res. Soc. Symp. Proc.* **2007**, *1002*, N03.
- [50] K. Tvingstedt, N.-K. Persson, O. Inganäs, A. Rahachou, I. V. Zozoulenko, *Appl. Phys. Lett.* **2007**, *91*, 113514.
- [51] T. D. Heidel, J. K. Mapel, M. Singh, K. Celebi, M. A. Baldo, *Appl. Phys. Lett.* **2007**, *91*, 093506.
- [52] N. C. Lindquist, W. A. Luhman, S.-H. Oh, R. J. Holmes, *Appl. Phys. Lett.* **2008**, *93*, 123308.
- [53] M. Zeman, J. Krc, *J. Mater. Res.* **2008**, *23*, 889.
- [54] M. Burgelman, J. Verschraegen, S. Degrave, P. Nollet, *Prog. Photovoltaics* **2004**, *12*, 143.
- [55] F. J. Beck, A. Polman, K. R. Catchpole, *J. Appl. Phys.* **2009**, *105*, 114310.
- [56] S. P. Sundararajan, N. K. Grady, N. Mirin, N. J. Halas, *Nano Lett.* **2008**, *8*, 624.
- [57] H. W. Gao, J. Henzie, M. H. Lee, T. W. Odom, P. Natl. Acad. Sci. USA **2008**, *105*, 20146.

- [58] G. H. Chan, J. Zhao, E. M. Hicks, G. C. Schatz, R. P. van Duyne, *Nano Lett.* **2007**, *7*, 1947.
- [59] A. C. Hryciw, Y. C. Jun, M. L. Brongserma, *Opt. Exp.* **2009**, *17*, 185.
- [60] A. D. Yaghjian, *IEEE Trans. Antennas Propag.* **2007**, *55*, 1495.
- [61] E. H. Sargent, *Adv. Mat.* **2005**, *17*, 515.
- [62] N. G. Anderson, *J. Appl. Phys.* **1995**, *78*, 1850.
- [63] K. Noone, D. S. Ginger, *ACS Nano* **2009**, *3*, 261.
- [64] I. Gur, N. A. Fromer, M. L. Geier, A. P. Alivisatos, *Science* **2005**, *310*, 462.
- [65] D. Pacifici, H. J. Lezec, H. A. Atwater, *Nat. Photonics* **2007**, *1*, 402.
- [66] J. P. Clifford, K. W. Johnston, L. Levina, E. H. Sargent, *Appl. Phys. Lett.* **2007**, *91*, 253117.
- [67] J. M. Luther, M. Law, M. C. Beard, Q. Song, M. O. Reese, R. J. Ellingson, A. J. Nozik, *Nano Lett.* **2008**, *8*, 3488.
- [68] A. Hagfeldt, M. Gratzel, *Acc. Chem. Res.* **2000**, *33*, 269.